Can DC Motors Directly Drive Flapping Wings at High Frequency and Large Wing Strokes?

Domenico Campolo, Muhammad Azhar, Gih-Keong Lau, and Metin Sitti, *Senior Member, IEEE*

Abstract—This paper proposes and experimentally validates a method for driving flapping wings at large wing strokes and high frequencies with a DC motor, based on direct, elastic transmission. The DC motor undergoes reciprocating, rather than rotary, motion avoiding the use of nonlinear transmissions such as slider-crank mechanisms. This is key to compact, easy to fabricate, power efficient, and controllable flapping mechanisms. First, an appropriate motor based on maximum power transfer arguments is selected. Then, a flapping mechanism is prototyped and its experimental performance is compared with simulations, which take into account the full dynamics of the system. Despite inherent nonlinearities due to the aerodynamic damping, the linearity of the direct, elastic transmission allows one to fully exploit resonance. This benefit is best captured by the *dynamic efficiency*, close to 90% at larger wing strokes in both experimental data and simulations. We finally show a compact flapping mechanism implementation with independent flapping motion control for the two wings, which could be used for future autonomous micro-aerial vehicles.

Index Terms—Bioinspired, dc motor selection, direct elastic transmission, resonant wings.

I. INTRODUCTION

RECENT years have witnessed an increase of research efforts in what is generally referred to as biomimetic robotics. Attracted by the unmatched performance of living systems, roboticists have started applying design principles drawing inspiration from biological evidence. In particular, agility and maneuverability in air of living flyers has inspired the development of an increasing number of so-called micro-aerial vehicles (MAVs) [1], [2]. Besides bio-inspired sensing capabilities and neuroinspired forms of controllers [3], there has been a technological push toward the development of biomimetic forms of propulsion, with particular emphasis on flapping wings. Flapping locomotion is superior to other forms of propulsions es-

pecially at lower speeds. Unparalleled by man-made vehicles, animals such as birds, bats, and insects are in fact capable of fast forward motion as well as hovering, which is one of the most energetically challenging forms of locomotion since it cannot exploit the accumulated kinetic energy of the body as in forward swimming/flying [4].

Efficient power usage is fundamental for the development of flapping propellers. One of the limits to flapping propulsion, also faced by living systems especially at larger size, is represented by the inertia of the wings. The need to periodically accelerate/decelerate the inertia of the appendices poses serious constraints to the flapping modality. Although the primary interest is doing work against the air, as this directly translates into production of lift and thrust forces, it is not uncommon that accelerating/decelerating wings at relatively high frequencies might require much larger inertial torques than damping ones. This would lead to oversized muscles (and actuators for artificial systems).

A first biological observation concerns the fundamental role played by *resonance*, physiologically induced by the structural elasticity typically inherent to the biomechanical properties of muscles and, for insects, of the external cuticle. The presence of elastic components for storage and release of the kinetic energy of the wings avoids the unnecessary waste of inertial power [4]. Indeed, such a principle has been successfully adopted in the design of flapping wings for robotic applications [5]–[7].

As emphasized by Baek *et al.* [7], at the smallest scales, the principle of mechanical resonance is widely implemented, in artificial systems, because elasticity is inherently present in both structures and actuators. On the other hand, at larger scales, where DC motors become a convenient choice for designers, the resonance principle is "almost forgotten." The reason is that most approaches, e.g., see the "DelfFly" [8], typically deploy slider-crank mechanisms to generate reciprocating motion from the DC motor rotary motion. Few attempts have been made to recover energy via an elastic element [7], [9], but the nonlinearity of the transmission reduces the benefits of resonance. From a controllability perspective, a drawback of conventional slider-crank-based wing flappers is that, once the mechanism is designed, the possible wing angles are in fact fixed and the only control parameter is the motor speed, allowing one to vary the flapping frequency but neither the wing stroke nor the mean flapping angle. In previous work [10], we showed how independent control of these parameters is beneficial for controllability of an autonomous, two-winged flyer. In fact, flapping frequency directly affects the average lift, while rolling torques can be generated by asymmetric wing strokes and pitching torques can be generated by shifting the wing strokes along the flapping plane by changing the average flapping angle.

D. Campolo, M. Azhar, and G.-K. Lau are with the School of Mechanical and Aerospace Engineering, Nanyang Technological University, Singapore 639798 (e-mail: d.campolo@ntu.edu.sg; MUHAMMAD138@ntu.edu.sg; MGKLau@ntu.edu.sg).

M. Sitti is with the Department of Mechanical Engineering, Carnegie Mellon University, Pittsburgh, PA 15213 USA (e-mail: sitti@cmu.edu).

The objective of this paper is to investigate a novel use of rotary DC motors for direct driving flapping wings at resonance, without using nonlinear transmissions such as slider-crank mechanisms. The use of an elastic mechanism, tuned to resonate with the wings/motor inertia, will relieve the motor from generating the high torques required to accelerate/decelerate the wings/motor inertia. We specifically focus on *hovering*, one of the most power-demanding forms of locomotion and for which the benefits of resonance can be mostly appreciated. Although the proposed principle is general and applicable at all scales, this project shall mainly target 10-g flyers, which are comparable in size and weight with small hummingbirds for which a large body of biological observation exists. As such, our main specification will be flapping frequencies in the range of 20–40 Hz and wing strokes as large as $\pm 60°$.

In the following, we shall first introduce a simplified aerodynamic model, which allows taking into account the nonlinearities of aerodynamic damping without delving into complex fluid dynamics approaches. Based on a second biological observation that wing motion in real flyers is "quasi-sinusoidal," a simplified analysis is applied to represent aerodynamic damping as a (nonlinear) equivalent electrical impedance. Maximum power transfer arguments are used to select a motor, based on impedance matching.

We then describe the development of a prototype, emphasizing the implementation details which avoid the introduction of unnecessary nonlinearities in the system dynamics, besides the inherent nonlinear aerodynamic damping. We characterize the prototype and compare the experimental data with simulations which take into account the full dynamics of the system. We finally show a compact implementation which is a suitable candidate for a future, autonomous MAV.

Along with this paper, a video is provided which shows fabrication details as well as the operation of the two prototypes in both real time and slow motion.

II. MODELS AND SIMPLIFIED ANALYSIS AT QUASI-SINUSOIDAL REGIME

A. Wing Aerodynamics: Nonlinear Damping

When a wing moves in a surrounding fluid, energy is transferred to the fluid and reaction forces arise. In principle, the force distribution on the wing may be derived from the Navier–Stokes equations. In practice, accuracy of the solutions to this problem is guaranteed only by numerical approaches. However, when accuracy requirements are not so stringent, reliable simplifications can be used which are based on the assumption of steady or quasi-steady flow [11]. Such models are based on quasi-steady blade element analysis, whereby the wing is assumed to be divided into a finite number of strips and each is analyzed independently.

For a wing of length R, blade element analysis considers infinitesimal strips at distance r from the *fulcrum* and of infinitesimal area $c(r)\,dr$, where $c(r)$ is the wing chord which determines the geometric profile.

For each section, the *instantaneous* drag torque is

$$dB = \frac{1}{2}\rho C_D\, r\, (r \cdot \omega)^2\, \text{sign}\,(\omega)\, c(r)\, dr$$
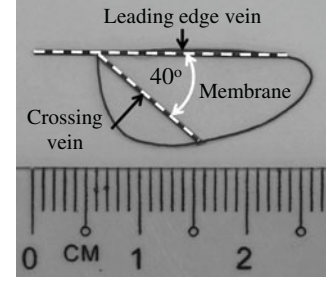

Fig. 1. Artificial wing used in our experiments. Based on Zhao *et al.* [13], a crossing vein at 40° with the leading edge was introduced to ensure rigidity of the wing.

where ρ is the density of the fluid (for air $\rho = 1.2$ kg/m^3), C_D is the adimensional drag coefficient, and $r \cdot \omega$ is the linear velocity of the section. C_D depends on the angle of attack (i.e., inclination of the wing/fin with respect to the fluid velocity), therefore is in principle time dependent and can be averaged out throughout the motion [12].

For a given wing, the aforementioned equations can be integrated over the whole wing length, leading to

$$B(\omega) = \int_0^R dB = B_0\omega^2\, \text{sign}\,(\omega) \qquad (1)$$

where the torque damping coefficient B_0 is defined as

$$B_0 = \frac{1}{2}\rho\, C_D \int_0^R r^3 c(r)\, dr. \qquad (2)$$

In this paper, we target small hummingbird wings, such as the one in Fig. 1, flapping at approximately 35 Hz. Fabrication details for the wings will be given later on. Here, we just mention that, based on the geometry and material properties of the fabricated wings shown in Fig. 1, the damping coefficient B_0 in (2) and the inertia J_w for a single wing (in our experiments we will use two wings) were numerically evaluated to be

$$B_0 = 1.32 \cdot 10^{-9}\ \text{kg m}^2\,\text{rad}^{-2} \qquad (3)$$

$$J_w = 9.53 \cdot 10^{-9}\ \text{kg m}^2. \qquad (4)$$

B. Analysis at Quasi-Sinusoidal Regime

Following [14] and based on biological observations [12], [15], *quasi-sinusoidal regime* assumptions allow estimating power requirements at steady state for a given stroke angle $\pm\theta_0$ and a given flapping frequency f_0. Wing kinematics (i.e., angular position, velocity, and acceleration) can be expressed as

$$\tilde{\theta} = \theta_0 \sin(2\pi f_0 t) \qquad (5)$$

$$\tilde{\omega} = \Omega_0 \cos(2\pi f_0 t) \qquad (6)$$

$$\tilde{\alpha} = -2\pi f_0 \Omega_0 \sin(2\pi f_0 t) \qquad (7)$$

where Ω_0 denotes the angular speed amplitude

$$\Omega_0 := 2\pi f_0 \theta_0. \qquad (8)$$

By introducing the concept of equivalent proportional damping,[1] the power dissipated against drag can be estimated as

$$\tilde{P}_{\text{drag}} = \tilde{B}(\tilde{\omega})\tilde{\omega} = B_0 \frac{8}{3\pi} \Omega_0 \tilde{\omega}^2 \qquad (9)$$

with a *peak* power (equivalent to the power amplitude)

$$P_{\text{drag}} = \left| \tilde{P}_{\text{drag}} \right| = B_0 \frac{8}{3\pi} \Omega_0^3. \qquad (10)$$

III. DC MOTOR SELECTION VIA IMPEDANCE MATCHING

Unlike gliding, hovering is very challenging from an actuator perspective. For wing strokes of $\pm 60°$, the inertial to aerodynamic torque ratio, for quasi-sinusoidal motions, can be quickly estimated to be

$$\frac{\tilde{\tau}_{\text{inertial}}}{\tilde{\tau}_{\text{aero}}} = \frac{J_w (2\pi f_0)^2 \theta_0}{B_0 (2\pi f_0 \theta_0)^2} = \frac{J_w}{B_0 \theta_0} \approx 6.9. \qquad (11)$$

Therefore, torques required to accelerate/decelerate the wing inertia are much larger than aerodynamic torques. For an actuator to drive a wing, the minimum requirement is to produce at least the same amount of power which is dissipated by the aerodynamic damping. If the actuator is also required to handle the peak inertial torques (e.g., five times higher than the aerodynamic ones), then the motor selection would necessarily lead to an oversized actuator, i.e., with a rated power which is much larger than the minimum aerodynamic requirements.

A. Simplified Analysis at Quasi-Sinusoidal Regime

In the case of quasi-sinusoidal kinematics, as for hummingbirds, exploiting resonance using a spring to resonate with the wing inertia at the desired frequency (f_0) can be extremely advantageous, also in presence of nonlinearities such as aerodynamic damping. To this end, let us consider a wing with inertia J_w, subject to aerodynamic damping $B(\omega)$, attached to a torsion spring with rotational stiffness K, and directly driven by a DC motor exerting a torque τ_m. This is captured by the following second-order system

$$J_w \alpha + B(\omega) + K\theta = \tau_m. \qquad (12)$$

The electromechanical model of a DC motor driving the mechanical system (12) can be written[2] as

$$\begin{cases} V = R_0 I + k_a \omega \\ k_a I = J_{\text{tot}} \alpha + (b_0 + B_0 \omega \, \text{sign}(\omega)) \omega + K\theta \end{cases} \qquad (13)$$

where V and I are, respectively, the voltage and current at the motor terminals; ω and α are, respectively, the angular speed and the angular acceleration of the rotor; R_0 is the electrical resistance of the armature; k_a is the armature constant; b_0 is the damping constant due to the internal friction (motor bearings); $J_{\text{tot}} := J_m + 2 \times J_w$ accounts for both rotor J_m and wings inertia $2 \times J_w$.

---

[1] For a given amplitude of a sinusoidal trajectory, an equivalent linear damper dissipates the same power as the nonlinear damper in (1), see [14].

[2] The armature inductance is neglected as the electrical dynamics are much faster than the mechanical ones, see [14].

Resonance can be set to occur at frequency f_0 by selecting the appropriate value K for rotational stiffness

$$K = (2\pi f_0)^2 J_{\text{tot}} \qquad (14)$$

then at sinusoidal regime, using (5)–(7), the inertial torque and the elastic torque will balance one another $J_{\text{tot}} \tilde{\alpha} + K\tilde{\theta} = 0$.

At resonance, sinusoidal voltage and current inputs of amplitude, respectively, V_0 and I_0 can be expressed as functions of Ω_0 as follows:

$$\begin{cases} V_0 = R_0 k_a^{-1} \left(b_0 + \frac{8}{3\pi} B_0 \Omega_0 \right) \Omega_0 + k_a \Omega_0 \\ I_0 = k_a^{-1} \left(b_0 + \frac{8}{3\pi} B_0 \Omega_0 \right) \Omega_0. \end{cases} \qquad (15)$$

Of course, for a given kinematics Ω_0, theoretical values for voltage and current amplitude can always be found from (15) but these might exceed the rated limits. Based on a recent method presented in [14], a power analysis will be developed which allows us to graphically select appropriate motors.

B. Power Estimates

The instantaneous power balance can be obtained from (15) and can be rewritten to highlight the power dissipated against mechanical damping (input electrical power minus electrical losses, see [14]):

$$\tilde{P}_{\text{mech}} \stackrel{\text{def}}{=} \tilde{V}\tilde{I} - R_0 \tilde{I}^2 = \frac{1}{\eta_x} \tilde{P}_{\text{drag}} \qquad (16)$$

where $\tilde{P}_{\text{drag}}$ is as in (9), and the efficiency η_x is defined as

$$\eta_x = \left(1 + \frac{b_0}{\frac{8}{3\pi} B_0 \Omega_0} \right)^{-1}$$

to take into account the mechanical power dissipated against friction instead of aerodynamic drag.

The maximum power transfer theorem for linear networks states that, for a given nominal input voltage, the maximum mechanical power delivered to the load equals the electrical losses, leading to a maximum 50% efficiency which can only be achieved in the case of *impedance matching* condition.

A similar result can be derived here, following [14]. The instantaneous mechanical power balance (16) can be written as

$$\eta_x \frac{1}{2} \frac{V_0^2}{2R_0} = \frac{1}{\mu} P_{\text{drag}} \qquad (17)$$

where P_{drag} is given in (10), R_{mech} is the *equivalent mechanical resistance*, μ is the *impedance mismatch* factor and are defined, respectively, as

$$R_{\text{mech}} := \frac{\eta_x K_a^2}{\frac{8}{3\pi} B_0 \Omega_0} \qquad (18)$$

$$\mu := 4 \frac{R_{\text{mech}}/R_0}{(1 + R_{\text{mech}}/R_0)^2}. \qquad (19)$$

Note that $0 < \mu \leq 1$ for all $R_0, R_{\text{mech}} > 0$ and also that $\mu = 1$ if and only if $R_0 = R_{\text{mech}}$, meaning that the power dissipated across R_{mech} equals the power dissipated across R_0, i.e., a 50% efficiency. In the best case scenario (i.e., impedance matching condition $R_{\text{mech}} = R_0$), the total input power is $\tilde{V}^2/(2R_0)$ and only half of it can be transferred to the mechanical load.

TABLE I
MOTOR PARAMETERS FROM PRECISION MICRODRIVES LTD. [16]

	model	weight grams	V_0 V	n_0 rad/sec	T_{stall} mNm	P_{max} mW	I_0 mA	I_{stall} mA	K_t mNm/A	R_0 Ω	b_0 nNm·sec/rad
1	104-001	0.5	3	5236	0.03	39	16	70	0.4	42.9	13.1
2	104-003	0.8	1.3	3037	0.04	30	14	90	0.4	14.4	20.5
3	106-001	1.4	1.3	2513	0.14	88	30	340	0.4	3.7	47.7
4	107-001	2.4	1.5	994.8	0.25	62	20	170	1.5	8.8	29.6
5	108-004	3.7	3	1885	0.93	438	50	600	1.6	5	41.1
6	108-005	2.5	3	1885	0.72	339	46	450	1.6 (**1.3***)	6.7 (**8.8***)	39.0
7	110-001	3	3	1623.1	0.5	203	40	300	1.7	10	41.1
8	110-002	3.7	1.5	1361.4	0.58	197	70	750	0.8	2	39.8
9	110-003	4.9	1.3	994.8	0.37	92	40	390	0.9	3.3	38.1
10	112-001	8	2.4	1675.5	1.55	649	150	1250	1.2	1.9	111

(*) Actual values as measured from a specific ì108-005 " model.

The advantage is that (17) provides an interpretation in terms of power and leads to a graphical representation useful for motor selection, as we shall see next.

C. Impedance Matching and Motor Selection

Each term in (17) is a function of the desired kinematics Ω_0, defined in (8) based on a desired stroke angle θ_0 and a desired flapping frequency f_0. The power P_{drag} to be dissipated against aerodynamic damping is the minimum amount that the motor should be able to deliver. In fact, the *required power* to be delivered could be even larger in case of impedance mismatch $\mu < 1$, as indicated by the right-hand side of (17). The left-hand side of (17) represents the *available power*, corresponding to the maximum power that can be transferred to an optimally matched load, i.e., one half of $V_0^2/(2R_0)$, further reduced by inefficiencies due to friction (η_x).

The right-hand side of (17) does not depend on motor parameters and only reflects requirements of the load (the flapping wing). The left-hand side of (17) is motor-specific and, for each Ω_0, it is possible to determine whether the operating conditions exceed any given limit, see [14] for details.

Considering a pair of wings, each similar to the one in Fig. 1, a mechanical inertia $J_w = 2 \times 9.53 \cdot 10^{-9}\,\mathrm{kg\,m^2}$ and aerodynamic damping $B_0 = 2 \times 1.32 \cdot 10^{-9}\,\mathrm{kg\,m^2\,rad^{-2}}$ can be estimated, as in (3) and (4). For a desired stroke angle $\theta_0 = \pm 60°$ and flapping frequency $f_0 = 35$ Hz, the speed amplitude can be determined to be $\Omega_0 = 2\pi f_0 \theta_0 = 230.3$ rad/s.

As possible actuators, we focused on commercially available, low-cost DC motors. Although this type of motor is widely available, e.g., for the toy industry, very few manufacturers provide detailed electromechanical characteristics. Among the few possible choices, we selected DC motors manufactured by Precision Microdrives Ltd. [16] and the relevant characteristics for each model are reported in Table I.

Fig. 2 graphically represents (17) on a power versus impedance ratio plot. The right-hand side of (17), i.e., the required power, is represented by the U-shaped curves for three different stroke angles at 35 Hz. In particular, we are interested in the thickest curve, i.e., $\pm 60°$ stroke angle. The left-hand side of (17), i.e., the available power, is represented by a line for each motor (identified by the number on top of the line which corresponds to the first column in Table I). The intersection of a motor line with a specific U-shaped curve identifies the power required to resonate the wing at a specific stroke angle
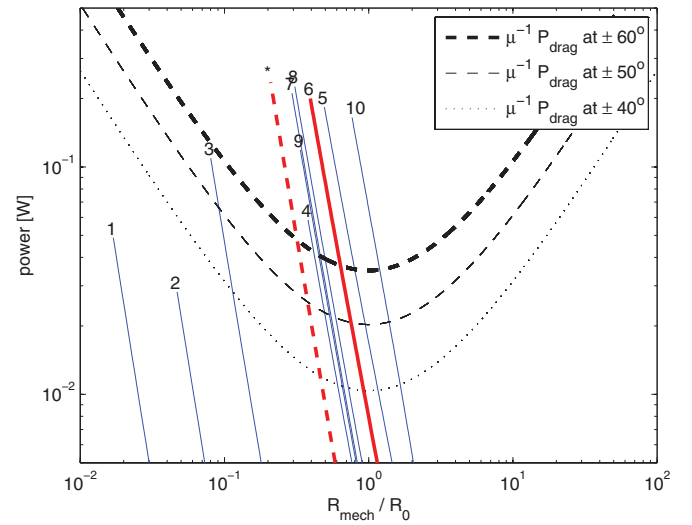

Fig. 2. Power versus impedance ratio plot. U-shaped curves represent required power for different stroke angles (at 35 Hz). Solid lines represent available power for specific motors (each identified by a number).

and frequency. A motor line graphically terminates whenever any operation limit occurs, as per datasheets. Therefore, the intersection between a motor line and a load curve always identify an operating condition within the rated limits of the motor. In our case, we are only operating points within the rated voltage, as this is the only limit available from the datasheets, but more general constraints could be introduced, see [14] for details.

Fig. 2 clearly shows the advantage of selecting motors with optimal impedance match, i.e., R_{mech} as close as possible to R_0, in order to minimize the required power and not to oversize the motor itself.

The lines relative to motor models "108-004," "108-005," and "112-001" (respectively, lines "5," "6," and "10" in Fig. 2) intersect the desired U-shaped curve relative to $\pm 60°$ stroke angle around its minimum level of required power. From Table I, the motor model "112-001" is rather heavy, while the remaining models weight only 2.6 g and are more suitable to be embedded in hummingbird-sized robots, in future applications. Between the "108-004" and the "108-005" model, we selected the latter for a specific mechanical feature, i.e., the shaft is accessible on both sides of the motor. This mechanical feature will be very important in the development of a prototype, as detailed in the next section.
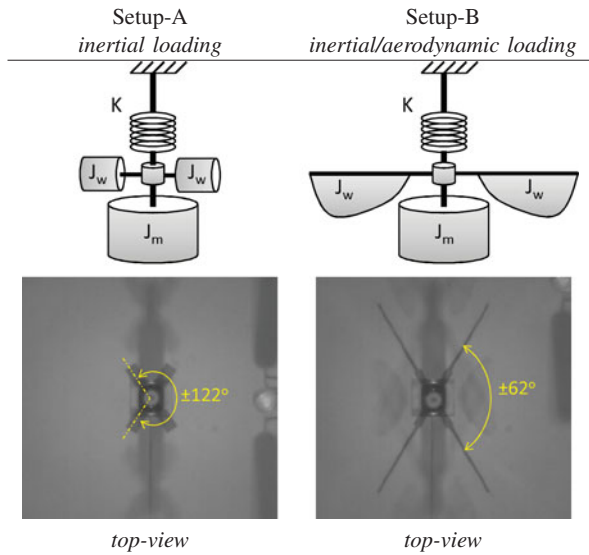
Fig. 3. (Top) Schematic drawings for the Setup-A and Setup-B configurations. (Bottom) Top views from a high-speed camera of the two actual setups while in operation. In both cases, two snapshots relative to the extreme angular positions are superimposed while the devices are being driven with a 2-V amplitude sinusoidal input voltage.

The thick line in Fig. 2 is relative to the selected model ("108-005") and based on the typical values. After this model was selected and purchased, we characterized the actual model and the dashed line in Fig. 2 is based on the experimental values (indicated in bold in Table I).

IV. MATERIALS AND METHODS

In order to test whether a DC motor is able to efficiently flap wings in presence of nonlinear aerodynamic damping, at high frequency and large wing stroke, we developed two setups, schematically represented in Fig. 3. Both setups consist of a DC motor (model "108-005," as selected in previous section) directly driving a load via an elastic transmission. In Fig. 3, the bottom cylinder schematically represents the rotor of the DC motor, with an estimated rotor inertia

$$J_m = 3.38 \cdot 10^{-9} \text{ kg m}^2. \tag{20}$$

For Setup-A, we used a purely inertial load consisting of two brass cylinders, designed to introduce a total inertia equal to $2 \times J_w$. For Setup-B, we used two similar wings (described later) which, in addition to a total inertia equal to $2 \times J_w$, introduce a nonlinear aerodynamic damping. In both cases, the load is balanced to minimize centrifugal forces and any resultant friction at the motor bearings.

In fact, both setups use the same motor and elastic transmission while the two different loads are interchangeable. The actual implementation of the system is visible in Fig. 4(b), showing when the wings are attached, and each component is described in the following sections.

Note: although not visible in Fig. 4(b), during normal operation, the stator of the DC motor is torsionally constrained, i.e., kept from turning. Without such a constraint, due to conservation of angular momentum, any angular acceleration of the rotor in one direction would induce a rotation of the stator in the opposite direction.

A. Wings

We used a pair of similar, artificial wings, as in Fig. 1, consisting of a membrane made of 102.5-μm cellulose acetate film and two veins made of 0.5-mm carbon fiber rod. The cross-sectional profile of the membrane is a flat plate and its platform is the scaled-down replication of the experimental wing used by Zhao *et al.* [13]. The root-to-tip distance and the maximum chordwise length are, respectively, 20 and 9 mm. The wings are plugged into a hollow wing-shaft connector that laterally pierces the upper string-shaft connector. For this, the leading edge vein is extended by a few millimeters. The other vein lies across the membrane at the angle of 40° with respect to the leading edge.

As the main purpose of this study is testing the ability of a DC motor to perform aerodynamic work against drag, the artificial wings are fixed at a 90° angle of attack.

The wing membrane and the wing veins are relatively thick compared to the size of the artificial wing. This combination is chosen to create a very stiff wing so that constant drag coefficient can be maintained when the prototype is being activated. A practical benefit of using rigid wings is relative to wing kinematic measurements. Fig. 3 (bottom) shows top views of the two setups as seen from a high-speed camera. For Setup-B, the wing appears as a rigid body at all times during motion.

As mentioned previously, the wing shape, including the 40° crossing vein, is a scaled-down version of the wing described by Zhao *et al.* [13]. Based on their characterization and for a fixed 90° angle of attack (as in our wing), we used the drag coefficient $C_D = 2.5$ and the damping coefficient was evaluated to be as in (3).

Based on the 2-D geometry and the properties of materials composing the wing, the moment of inertia of each wing with respect to the center of rotation is numerically estimated to be as in (4).

B. Elastic Transmission

While actuators and wings are natural elements for a flapping-winged robots, the elastic transmission is in fact the key and novel[3] component of the proposed mechatronic platform.

An elastic transmission, as only schematically represented in Fig. 3, can be implemented in many different ways. For characterization purposes, we opted to use wires as torsion springs to guarantee linearity of the stiffness coefficient for relatively large angular displacements (a $\pm 60°$ torsion induces relatively low strains in a sufficiently long wire) and to be able to easily adjust the values of stiffness to our needs by simply selecting appropriate wire lengths.

While the schematic drawing in Fig. 3 shows only one spring attached to the rotor of the DC motor, we implemented a symmetric structure whereas each side of the motor shaft is connected to a torsion spring (wire), as shown in Fig. 4(b). To properly behave as torsion springs, wires have to be in tension, although tension itself does not influence the torsion stiffness. Having equal tension on both sides of the shaft avoids any axial loading of the motor which would easily lead to prohibitive friction at the motor bearings. This is actually the reason for choosing a motor with the shaft accessible on both sides.

---

[3]At least for applications involving DC motors directly driving the load.
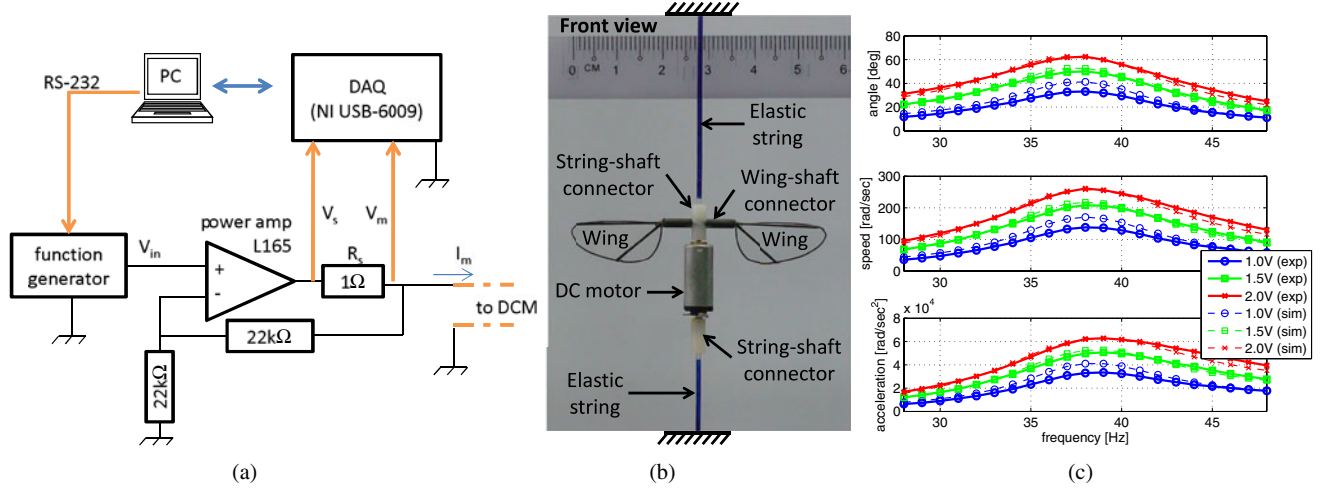
Fig. 4. (a) Actual prototype (front view) with wings attached (Setup-B). (b) Diagram of the electrical setup used for data acquisition (further details can be found in the supplementary video attachment). (c) Experimental and simulated kinematics (amplitude of angular position, angular velocity, and angular acceleration) versus frequency, in a range centered around mechanical resonance.

The two elastic strings in Fig. 4(b) are made of 1.024-mm clear nylon, but painted in blue ink to make them more visible, and the length of each one is 100 mm. For each nylon string, one end is fixed (mechanically grounded) and the other is secured to the tip of the motor shaft through a string-shaft connector.

Based on the geometry and the material properties of the two nylon strings and considering the range of possible values for Young's modulus of nylon strings, the expected torsion stiffness coefficient $K = 2 \times I_s G_s / l_s$ is in the range 1.5–$4 \cdot 10^{-3}$ N·m/rad, where I_s is the polar moment of inertia, G_s is the modulus of shear of elastic string, l_s is the length of string, and the $2\times$ factor accounts for the fact that two similar springs act in parallel on the motor shaft. The experimentally measured value for the overall stiffness was found to be in the lower end of the range

$$K = 1.6 \cdot 10^{-3} \text{ N·m/rad.} \tag{21}$$

C. Data Acquisition

The experiments with both setups consisted of 3×21 trials during which the motor was driven with sinusoids at different frequencies and different voltage levels. For each voltage level (1.0, 1.5, and 2.0 V), the frequency was swept in the range 28–48 Hz, with increments of 1 Hz. Each sinusoid would drive the setup for 1 s, to allow the system to be in steady state, after which the electrical variables V_s and V_m as well as the high-speed camera video would be recorded and stored for later processing. Using the circuit in Fig. 4(a), we directly measure the voltage V_m across the motor terminals as well as the voltage $V_s - V_m$ across the sensing resistor $R_s = 1\Omega$ in series [4] with the motor armature. From the latter, we can determine the current I_m in the motor $I_m = (V_s - V_m)/R_s$.

The whole procedure was automated by a MATLAB script used to set, over an RS-232 communication channel, the fre-

quency and voltage levels of a function generator as well as to start/stop the data logging from the data acquisition board (National Instrument USB-6009, 14-bit resolution, 10-kHz sampling rate).

At the same time, a high-speed camera (Photron Fastcam-X 1024 PCI) was used to record the wing motion (from a top view, as shown in Fig. 3) at 6000 frames/s.

D. Data Preprocessing

We processed the series of grayscale images by comparing, for each image, the next with the previous one, easily identifying the pixels in the image undergoing a change of intensity. Using an *ad hoc* threshold, we were able to isolate the pixels that were changing intensity due to the wing motion. These pixels are highlighted in the bottom-right snapshot of Fig. 3. A simple regression analysis of the coordinates of such pixels was then used to estimate the wing angle (superimposed straight line in the bottom-right snapshot of Fig. 3). The algorithm failed only when the velocity was close to zero, leading to misestimates in 3–4% of the images. These cases could be easily identified by the severe discontinuity of the estimate. After removing these artifacts, we numerically differentiated the signal to derive an estimate of the angular velocity $\omega^{\text{raw}}(t_i)$, where t_i is a discrete time relative to the 6000 frames/s sampling rate.

Due to the video processing and to the numerical differentiation, the velocity estimates were affected by high-frequency noise which requires some filtering. Since we are dealing by definition with periodic signals, we derived the discrete-time Fourier series coefficients α_n and β_n from the discrete-time signal $\omega^{\text{raw}}(t_i)$ and we filtered by only considering harmonics of order not higher than five [5] ($n \leq 5$), i.e., our time-continuous filtered signal is $\omega^*(t) := \sum_{n=1}^{5} \alpha_n \sin(2\pi n f_0 t) + \beta_n \cos(2\pi n f_0 t)$ where f_0 is the frequency of the input sinusoid driving the motor. Once α_n and β_n are known, the stroke angle

---

[4]The resistor R_s is not exactly in series but this is a realistic approximation as, from the circuit in Fig. 4(a), the current flowing through the two 22 kΩ resistors is $V_m/44 \text{ k}\Omega \leq 3 \text{ V}/44 \text{ k}\Omega = 68 \text{ }\mu\text{A}$, where 3 V is the maximum voltage across the motor terminals.

[5]Being interested in periodic signals with fundamental frequency around 35 Hz, we discarded harmonics higher than $175(= 5 \times 35)$ Hz.

and acceleration are easily computed as

$$\theta^*(t) := \frac{1}{2\pi f_0} \sum_{n=1}^{5} -\frac{\alpha_n}{n} \cos(2\pi n f_0 t) + \frac{\beta_n}{n} \sin(2\pi n f_0 t)$$

$$\alpha^*(t) := 2\pi f_0 \sum_{n=1}^{5} n\alpha_n \cos(2\pi n f_0 t) - n\beta_n \sin(2\pi n f_0 t).$$

A similar filter was applied to the electrical variables, i.e., voltage and current at the motor terminals.

E. Simulations

Along with the experiments, we performed simulations of the whole system taking into account the nonlinearities of the second-order mechanical system (12) as well as the full system dynamics of the DC motor (13), including the effects of the armature inductance. In particular, for the numerical simulations, we did not apply any simplifying assumptions. We used the ode45 function in the MATLAB environment which returns also the transient analysis. As we were interested in steady-state solutions, starting from an arbitrary zero state vector,[6] we simulated exactly one time period. The final conditions were then used as initial conditions for a subsequent simulation and the whole process was reiterated until the final conditions were deemed close enough (by an arbitrary threshold) to the newest initial conditions. Only few iterations were necessary to obtain approximately periodic solutions of (12) and (13). At this point, the same analysis was carried out for both the experimental data and simulations, as described next.

V. EXPERIMENTAL DATA ANALYSIS AND MODEL PREDICTIONS

A. Experiments With Purely Inertial Loads (Setup-A)

The purpose of the experiments conducted on Setup-A was to verify the reliability of the electromechanical model (13) of the motor. Among the various estimated parameters needed to predict the behavior of the full system (13), the aerodynamic damping coefficient B_0 is the least reliable. The purely inertial load used for Setup-A has a negligible aerodynamic damping; therefore, the only damping comes from the friction at the motor bearing.[7] The bottom-left picture in Fig. 3 shows two superimposed snapshots (top views) of the Setup-A, representing the two extreme angular positions of the load when the motor was driven with a 1.0 V sinusoidal input (note: this is much lower than the rated 3.0-V voltage). As clear from the snapshot, the system undergoes approximately a $\pm 55°$ wing stroke which is perfectly in line with the model prediction. It should be noticed that the output kinematics are exactly the target kinematics for the final application, although very low voltage was required due to the low friction.

B. Experiments With Wings (Setup-B): Output Kinematics

Unlike for the purely inertial load (Setup-A experiments), when wings were flapped, the model predicted higher displacements than those experimentally measured, meaning that the damping coefficient B_0 in (3) is underestimated.

By simply adjusting the value of B_0, it was not possible to match experimental and simulation results for all amplitudes. Since a realistic estimation of this coefficient is important to infer the power dissipated against the aerodynamic damping, as detailed later, we heuristically selected a value for B_0 which would at least match the experimental data in the range of desired kinematics, i.e., $\pm 60°$ wing stroke. This specific value is

$$B_0^* := 2.05 \cdot 10^{-9} \text{ kg m}^2 \text{ rad}^{-2} \tag{22}$$

with a $2\times$ factor to account for both wings. This matching is shown in Fig. 4(c) to be quite accurate for the target amplitude ($\pm 60°$) but, at lower amplitudes, the model still predicts large motions than the actual ones. This amplitude-dependent difference clearly highlights a nonlinear behavior. Since the major nonlinearity is due to the aerodynamic damping, the fact that the model cannot match the experiments at all amplitudes is indicative of the degree of simplifications behind the quasi-steady blade element analysis which led to (1).

Theoretical predictions and experimental results agree in that resonance is relatively independent of the input amplitude. In this sense, it is possible to modulate the flapping amplitude without affecting the flapping frequency, i.e., maintaining the resonance condition. It is also important to notice that any dc offset in the input voltage translates into an offset in the mean flapping angle.[8] The possibility to independently control flapping frequency, wing stroke, and mean flapping angle is important for control purposes, as discussed later.

C. Inverse Dynamics, Power Analysis, and Dynamic Efficiency

While measuring kinematics is straightforward, measuring forces is technologically more challenging. For this reason, we shall resort to indirect torques estimation from measured kinematics, also known as *inverse dynamics* analysis. To this end, we evaluated each single term in (12) which comprises inertial (τ_i^*), aerodynamic (τ_a^*), friction (τ_f^*), elastic (τ_e^*), as well as motor (τ_m^*) torques, defined as

$$\tau_i^*(t) := J_{\text{tot}} \, \alpha^*(t) \tag{23}$$

$$\tau_a^*(t) := B_0 \, \omega^{*2}(t) \, \text{sign}\,(\omega^*(t)) \tag{24}$$

$$\tau_f^*(t) := b_0 \, \omega^*(t) \tag{25}$$

$$\tau_e^*(t) := K\theta^*(t) \tag{26}$$

$$\tau_m^*(t) := \tau_i + \tau_a + \tau_f + \tau_e \tag{27}$$

recalling that the asterisk (*) denotes a truncated Fourier series containing harmonics up to the fifth order.

Once the kinematics is known and the various torques have been estimated via inverse dynamics, the instantaneous power can be estimated as torque times angular velocity. For dissipative

---

[6]We defined a 3-D state vector comprising motor current, wing angle, and wing velocity.

[7]The intrinsic damping of the nylon string is negligible with respect to the motor damping as easily tested with a torsion pendulum configuration, where the motor is replaced by a pure cylinder.

[8]The angular offset relative to a *constant* input voltage (dc offset) is T_{stall}/K, approximately $25°$ at nominal 3-V dc, from Table I and (21).

torques, such as aerodynamic damping and motor friction, the instantaneous power is by definition nonnegative and so is the average power.

When it comes to inertial and elastic torques, the instantaneous power is the time derivative of the kinetic energy $\frac{1}{2}J_{\text{tot}}\omega^{*2}$ and the elastic energy $\frac{1}{2}K\theta^{*2}$, respectively. Therefore, the average power is identically zero, being both energy functions periodic of period T.

In analyzing the "fitness" to fly of hovering animals such as hummingbirds, both Weis-Fogh [12] and Ellington [17] considered the work done by the muscles without accounting for its sign. For example, Ellington [17] defines the "mean inertial power" as the work done by muscles to accelerate wings from zero to maximum angular velocity during the first half of a half-stroke, i.e., a quarter of period. This is equivalent to the average of the norm of the instantaneous power, i.e., without considering its sign, which in the case of inertial torques becomes

$$\bar{P}_i^+ = \frac{1}{T}\int_0^T |\tau_i \cdot \omega|\, dt = \frac{\frac{1}{2}J_{\text{tot}}\omega_{\text{max}}^{*2}}{4T}.$$

We shall here follow a similar approach and consider the norm of motor power

$$\bar{P}_m^+ = \frac{1}{T}\int_0^T |\tau_m \cdot \omega|\, dt$$

since, also in the case of artificial "muscles" such as DC motors, the negative work done by a motor to decelerate a wing cannot be efficiently recovered at the electrical port of the motor, mainly due to the motor resistance [7].

Weis-Fogh [12] used a very effective graphical representation for computing the average power contributions due to the different sources (23)−(27). In fact, a simple change of variable in the integral

$$\int_0^T \tau \cdot \omega(t)\, dt = \int_{\theta(0)}^{\theta(T)} \tau\, d\theta$$

suggests that average power can be graphically represented as an area in a torque versus angle plot. Weis-Fogh used this plot to evaluate power contribution in the case of quasi-sinusoidal approximations. For more accurate calculations involving higher harmonics, we shall resort to numerical integration, although the graphical representation is still very effective to understand what happens beyond the quasi-sinusoidal approximation.

Fig. 5 shows the torque versus angle representation of the aerodynamic torque (τ_a), the friction torque (τ_f), and the elastokinetic torque ($\tau_i + \tau_e$), superimposing the experimental results in response to input voltage sinusoids with 2.0-V amplitude and different frequencies (between 28 and 48 Hz, with 1-Hz step). The algebraic sum of these components corresponds to the torque provided by the motor, as in (27). The areas underneath the curves correspond, for each frequency, to the average power (times the period T).

The curves for friction and aerodynamic damping are quasi-elliptical and enclose the largest area at resonance (thickest dashed line), i.e., in presence of larger wing strokes. It is clear how, near resonance, the power dissipated against aerodynamic damping is much larger than the one due to motor friction. The average aerodynamic power, for both experimental data
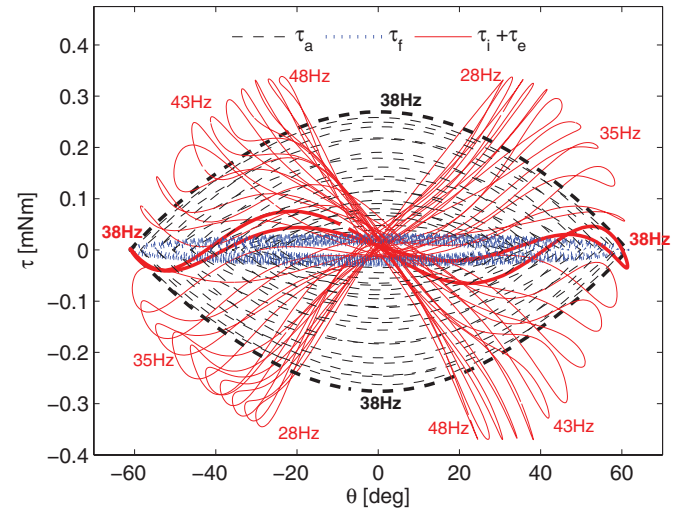

Fig. 5. Experimental torque versus wing angle plot in response to 2.0-V input sinusoids at different (superimposed) frequencies, between 28 and 48 Hz, with 1-Hz step. Elastokinetic torques ($\tau_i + \tau_e$) appear as "stretched loops," and labels indicate the loops relative to 28, 35, 38, 43, and 48 Hz. Aerodynamic torques appear as ellipses (the largest occurring at 38 Hz, as labeled). Thicker lines indicate resonance conditions, which in our system occurs at 38 Hz.
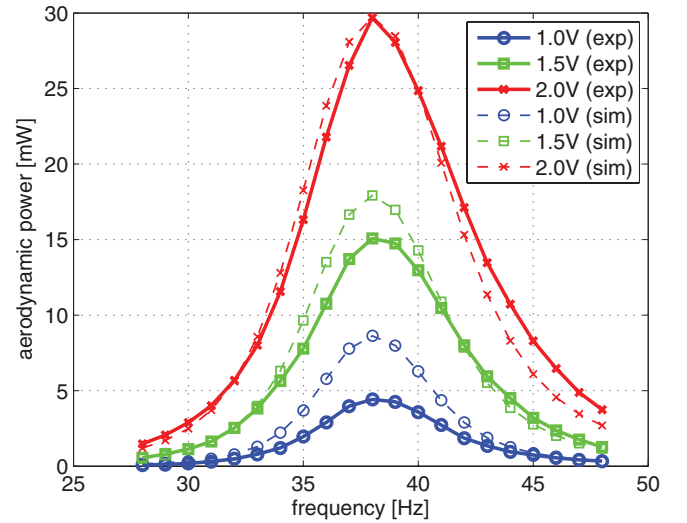

Fig. 6. Experimental (solid lines) and simulated (dashed lines) average aerodynamic power at different frequencies and at different input voltage levels (1.0, 1.5, 2.0 V, as denoted by the markers).

and simulations, is represented in greater details in Fig. 6, for different frequencies and different input voltages.

The curves relative to the elastokinetic torque appear in Fig. 5 (solid lines) as "stretched loops," rather than elliptical. To explain the origin of such "stretched loops," it is instructive to see what happens in a quasi-sinusoidal approximation. In this ideal case, the angular position ($\tilde{\theta}$) and the angular acceleration ($\tilde{\alpha}$) are perfectly in phase, as clear from (5) and (7). This means that, within a quasi-sinusoidal approximation, the elastokinetic torque $\tilde{\tau}_{ie}$ is also proportional to the stroke angle, by a factor

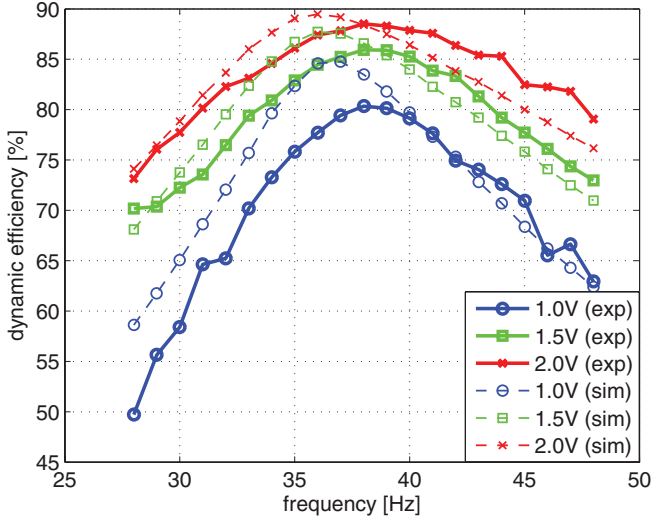$$\frac{\tilde{\tau}_{ie}}{\tilde{\theta}} = K - (2\pi f_0)^2 J_{\text{tot}}.$$

Fig. 7. Experimental (solid lines) and simulated (dashed lines) dynamic efficiency at different input voltages and different frequencies.

Fig. 8. Experimental (solid lines) and simulated (dashed lines) average input power at different input voltages and different frequencies.

It is clear that this proportionality is zero at resonance (14), positive at lower frequencies, and negative at higher frequencies. In this ideal case, at resonance, the elastic and the inertial torques perfectly balance one another and the motor needs only to overcome dissipative torques.

When higher harmonics are introduced, due to the nonlinear aerodynamic damping, the elastokinetic torque is no longer perfectly in-phase with the stroke angle, although a linear trend can still be observed. Nevertheless, the benefits of resonance are still visible, as the elastokinetic power at resonance (area underneath the thickest solid line) is still much lower than the aerodynamic power (area enclosed by the thickest dashed line).

Remark: The maximum motor torque (thick solid line in Fig. 5) is much smaller than the maximum aerodynamic torque (thick dashed line in Fig. 5), while without an elastic string, the inertial torques (entirely provided by the motor) would be five times larger, as shown previously.

The benefits of resonance are best captured by the so-called *dynamic efficiency*, defined as [12]

$$\eta_{\text{dynamic}} := \frac{\bar{P}_a}{\bar{P}_m^+} = \frac{\int_0^T \tau_a^* \cdot \omega^* \, dt}{\int_0^T |\tau_m^* \cdot \omega^*| \, dt} \quad (28)$$

which, at larger wing strokes, reaches values close to 90% for both experimental data and simulations, as shown in Fig. 7.

The dynamic efficiency is a measure of optimality which does not include the actuator properties. Therefore, it is important to analyze which percentage of the input power $\bar{P}_{\text{VI}}$ (e.g., coming from a battery) can be dissipated against the aerodynamic damping. This is what we here call overall efficiency and define as

$$\eta_{\text{overall}} := \frac{\bar{P}_a}{\bar{P}_{\text{VI}}} = \frac{\int_0^T \tau_a^* \cdot \omega^* \, dt}{\int_0^T V_m \cdot I_m \, dt}. \quad (29)$$

The input power, for all frequencies and input voltages, is represented in Fig. 8. It should be noticed how, at resonance, while the wing stroke increases, the input power actually decreases.
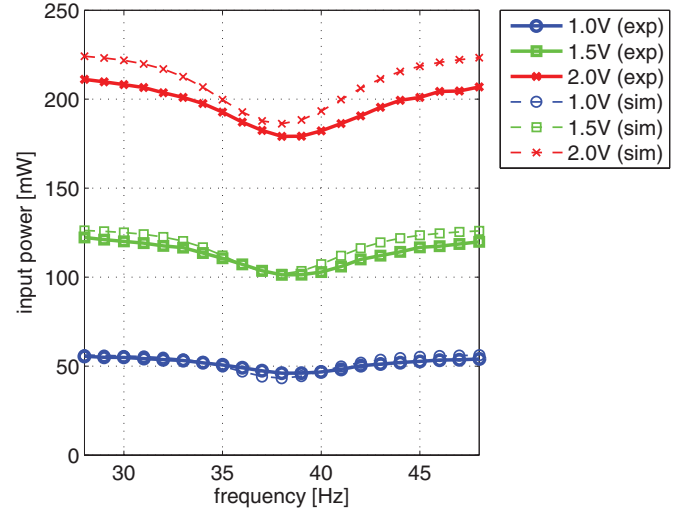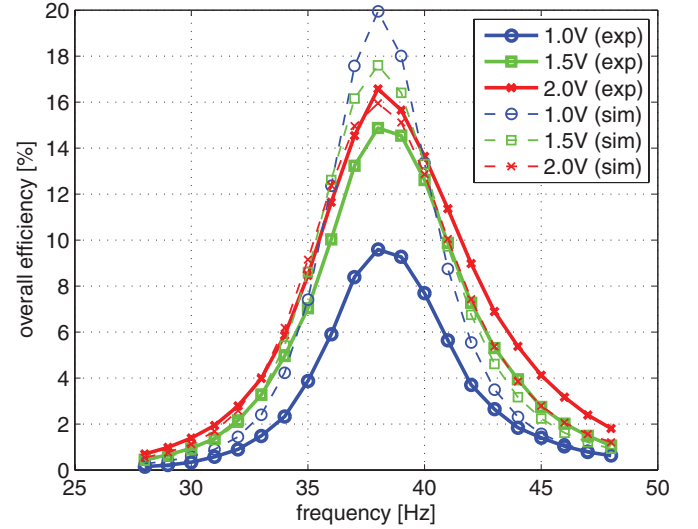

Fig. 9. Experimental (solid lines) and simulated (dashed lines) overall efficiency at different input voltages and different frequencies.

The overall efficiency is plotted, for all frequencies and input voltages, in Fig. 9. First, it should be noticed that in the best scenario, i.e., when the load impedance matches the load, we cannot hope for more than 50% overall efficiency since the remaining 50% of power is dissipated in the motor armature resistance. Second, the actual matching condition (thick dashed line in Fig. 2) is not optimal as predicted from the catalog data (thick solid line in Fig. 2). This leads to an overall efficiency of nearly 17% for the largest wing strokes, at resonance.

D. Flapping Wings Without The Benefits of Resonance

To test the ability of the motor to flap wings *without* the benefits of mechanical resonance, the elastic string was removed and the motor was driven with a sinusoidal voltage at 38 Hz, with the same voltage amplitude used in previous section, i.e.,
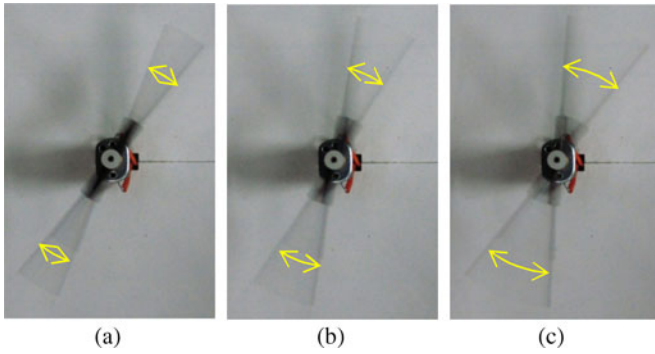
Fig. 10. Output wing motion *without* an elastic element in response to input sinusoids at 38 Hz and at different voltage levels. The top view snapshots were taken with a webcam; the wing stroke angle can be inferred by the blurring.
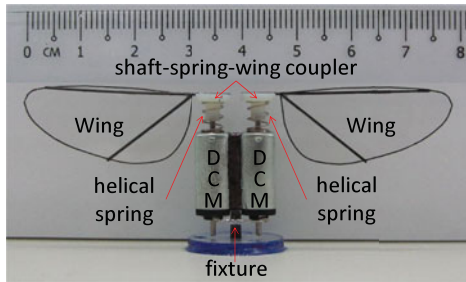

Fig. 11. New prototype with independent wings. Further details can be found in the supplementary video attachment.

1.0, 1.5, and 2.0 V. As expected, the motor is unable to produce large wing motions. Fig. 10 shows snapshots of the output wing stroke which, at the maximum input voltage, is no larger than $\pm 17°$ at 2.0 V.

As a note, since the string was removed, there was no equilibrium point and the average position drifted from trial to trial.

E. Suitability for Autonomous Vehicles

The platform shown in Fig. 4(b) is meant for characterization. Nylon strings are used as torsion springs to guarantee linearity of the stiffness coefficient at relatively large angular displacements and to be able to easily adjust the values of stiffness to our needs by simply selecting appropriate string lengths.

Of course, a different implementation would be required for a future, autonomous flying vehicle. In this sense, to test the potentiality of our approach, we also developed a compact and lightweight device, see Fig. 11, which shows similar performance as the one used for characterization. The main difference with the prototype in Fig. 4(b) is in the elastic structure, implemented with compact helical springs (MISUMI wire spring, model no. WFH4-5) attached between the rotor shaft and the stator.

A second difference is that we are now using two motors to implement proper wing flapping (in the setup in Fig. 4(b), the two wings are always coplanar). In fact, a single, larger wing is attached to each motor which can be flapped at the cost of some additional friction at the motor bearings, due to centrifugal axial loading, with minimal degradation of performance.

The operation of such a device is shown in the provided video, where the two motors are driven in parallel by a single amplifier. Alternatively, each motor could be driven by a different amplifier, leading to different kinematics for the left and right wings, useful from a control perspective.

Another possibility would be to have two motors, each driving two coplanar wings [as in our original setup in Fig. 4(b)], to implement an X-Wings configuration, which has been proved to be very effective in capturing clap-and-fling aerodynamic effects [18].

VI. DISCUSSION

In this section, we aim to discuss our results, also in relation to conventional approaches.

A. Second-Order Systems and Nonlinearities

The behavior of our system is described by the second-order differential equation (12) where the nonlinearity is solely due to the damping term (second term of the left-hand side), while the inertial and elastic terms (respectively, the first and the last term of the left-hand side) are linear. Linearity of the inertial term is guaranteed by the direct drive, while linearity of the elastic term is a consequence of implementing torsion springs via long and thin wires.

A first property of systems such as the one in (12) is that the resonant frequency is relatively independent of the nonlinear damping, as shown by our model prediction as well as experimental measurements at different input voltage amplitudes, in Fig. 4(c). This is not the case when the elastic term is nonlinear, which might give rise to undesirable "jump phenomena" and resonant frequency shifts, documented, for example, in [19].

A second property of systems such as the one in (12) is that, despite the nonlinear damping, solutions still maintain a quasi-sinusoidal regime, at least for sinusoidal forcing inputs, allowing for ac steady-state "quick estimates" as in [12]. Unlike direct drive, slider-crank mechanisms suffer from an inherent nonlinearity in the inertial term which reduces the benefits of resonance due to the nonnegligible presence of higher order harmonics, as shown in [7].

B. Power Considerations for Motor Selection

DC motors are rated by manufacturers based on dc steady-state operating conditions, i.e., assuming that voltage V, current I, speed ω, and torque T are constant. Operational limits provided by manufacturers are mainly meant to prevent overheating of the motor which is directly related to the average power, not the instantaneous power. For dc steady state, average power can be evaluated directly as the product of constant variables such as VI or $T\omega$. At ac steady state, the average power depends on the amplitude but also on the phase difference. For example, the average electrical power is evaluated as $\frac{1}{2}V_0 I_0 \cos \Phi$, where V_0 and I_0 are the amplitude of ac voltage and ac current, respectively, and Φ is the phase difference between them. The $\frac{1}{2}$ factor in the ac power formula means that the maximum operating conditions for variables such as, for example, voltage and current can have peak values higher than the nominal values,

i.e., than those rated by the manufacturer at the dc steady-state case, before exceeding the ultimate power limits which would cause overheating.

Remark: However, when operating at ac steady state, even before overheating might occur, current amplitudes beyond the nominal dc values might lead to magnetic saturation.

As for our selected motor (line "6" in Fig. 2), the rated 339-mW maximum power ($P_{\max}$ in Table I) clearly exceeds the required 30 mW (minimum level of the top U-shaped curve). This means that, in principle, a smaller motor would also be suitable but none of the lighter motors in Table I meets the 30 mW requirement, except for motor "4" which however displays very little safety margin in Fig. 2 (especially considering that actual parameters might differ from the values stated in the manufacturer's catalog, as for motor "6")

It is interesting to notice how motor '3' is actually sufficiently powerful (88 mW) but does not pierce the 30-mW curve due to an impedance mismatch. A possible solution would be to design an appropriate linear transmission (e.g., gear-head system) to ensure impedance matching, equivalent to shifting line "3" rightward in Fig. 2. Such a solution would, of course, increase complexity and reduce efficiency and will be addressed in future work.

C. Potential Benefits With Respect to Conventional Approaches

The main difference with conventional approaches based on nonlinear transmissions, such as slider-crank mechanisms, is in the reciprocating motion of the motor itself. A clear advantage of our approach is in the reduction of complexity: besides a motor and a wing, we only need a spring, making the system very robust and inexpensive. In our case, exploiting resonance is a necessity as it would be highly inefficient, if not impossible, to generate large wing strokes at high frequency without an elastic mechanism storing and releasing energy, as shown in Section V-D. Conventional approaches do not require an elastic mechanism, although they would indeed benefit from resonance [7]. However, due to inherent nonlinearities, the benefits of resonance cannot be fully exploited and it would be very interesting to compare, on a fair ground, the two approaches in terms of efficiency.

So far, we are only aware of the work of Baek *et al.* [7] on incorporating the energetics of voltage-driven DC motors in the overall analysis. However, to the authors' knowledge, an explicit efficiency analysis and a methodology for motor selection are still missing. Such an analysis is complicated by several factors. In our case, "quick estimates" (based on ac regime analysis), inspired by the work of Weis-Fogh [12] on flapping animal species, were possible because of the quasi-sinusoidal properties of the wing trajectories (a consequence of having nonlinearities only in the damping as mentioned earlier in this section). The regime analysis of DC-motor-driven slider-crank mechanisms must rely on numerical solutions, as speed and torque profiles are far from being quasi-sinusoidal [7].

Another advantage we see in our approach is that we can independently control wing beat, wing stroke, and mean flapping angle, with potential benefits for controllability of a two-winged platform [10]. For slider-crank mechanisms, only wing beat can be controlled, while wing stroke and mean flapping angle are fixed. Having frequency as the sole controllable parameter might lead to disadvantages especially when resonance is used to boost efficiency. A change in voltage amplitude, for purposes of control, would induce a change in frequency, and therefore, the system might end up operating out of resonance.

VII. CONCLUSION

In this paper, we experimentally demonstrated that DC motors, in concert with an elastic mechanism, can be used to *directly* drive flapping wings at large wing stroke and at high frequencies. The major novelty of our approach, to the authors' knowledge, is in that the DC motor undergoes a reciprocating (i.e., back and forth) rather than rotary motion. Whenever a reciprocating motion has to be generated from a DC motor, typical approaches make use of crank-arm mechanisms to turn the motor rotation into wing flapping. Crank-arm mechanisms unavoidably introduce nonlinear kinematics, which strongly limits the application of the bioinspired principle of mechanical resonance as a means of relieving the motor from excessive inertial loading. The use of a direct transmission and of an elastic mechanism ensures that the *sole* nonlinearity in the mechanical system (12) is in the aerodynamic damping. Resonance is still very effective in this type of nonlinear second-order system since solutions are "quasi-sinusoidal" and condition (14) implies that inertial and elastic torques balance one another, as in the case of linear systems.

In fact, besides mechanical resonance, "quasi-sinusoidal" motion is the second important lesson learned from biology. The method based on "quick estimates," as proposed by Weis-Fogh [12] to analyze the fitness to fly of several species, was readapted to DC motors, generalizing the maximum power transfer theorem to nonlinear systems at quasi-sinusoidal regime [14]. The aerodynamic damping of a given wing, at a given desired kinematics, is captured by the amplitude of the angular velocity Ω_0, defined in (8), and can be represented as an equivalent impedance R_{mech} in the electrical domain, defined as in (18). The DC motor is then selected by matching its armature resistance directly with the equivalent wing impedance.

In conclusion, we developed a prototype which served as a proof of concept. The selected motor was in fact able to drive the given wing at the desired kinematics, keeping well within the rated limits. The same task was clearly impossible when the elastic element was removed, as shown in Fig. 10. Although our work focused on miniature flying robots, the same concepts can be potentially extended to other applications where quasi-cyclic motions are important, such as running, swimming, and hopping robots.

As future work, although this novel method seems potentially useful in flying/hovering robots applications, further investigation is still required. In fact, so far, we only moved air and did not generate any lift. This was purposely done by setting the wing at a $90°$ angle of attack, in order to face maximum drag conditions. To be able to generate lift, we shall introduce an extra degree of freedom to allow wing rotation. Whether active or passive, this extra degree of freedom will influence the

motor. In particular, a second-order description as in (12) will no longer be sufficient. Up to which extent the motor selection method will still be valid in this new scenario shall also be investigated. Furthermore, although suitable for "quick estimates" of the power to be handled by a motor, our approach rests on simplified aerodynamic models. Especially, if wing rotation is allowed in addition to flapping, complexity behind lift generation mechanisms might require numerical solvers, based on Navier–Stokes formulation, to provide better estimates.

REFERENCES

[1] J. Ayers, J. L. Davis, and A. Rudolph, Eds., *Neurotechnology for Biomimetic Robots*. Cambridge, MA: MIT Press, 2002.

[2] Y. Kawamura, S. Souda, S. Nishimoto, and C. P. Ellington, "Clapping-wing micro air vehicle of insect size," in *Bio-mechanisms of Swimming and Flying: Fluid Dynamics, Biomimetic Robots, and Sports Science*, N. Kato and S. Kamimura, Eds. New York: Springer-Verlag, 2008, vol. 3, pp. 319–330.

[3] D. Lachat, A. Crespi, and A. J. Ijspeert, "BoxyBot: A swimming and crawling fish robot controlled by a central pattern generator," in *Proc. 1st IEEE/RAS-EMBS Int. Conf. Biomed. Robot. Biomechatron.*, Pisa, Italy, Feb. 20–22, 2006, pp. 643–648.

[4] T. Weis-Fogh, "Energetics of hovering flight in hummingbirds and in drosophila," *J. Exp. Biol.*, vol. 56, no. 1, pp. 79–104, 1972.

[5] T. Yasuda, I. Shimoyama, and H. Miura, "Microrobot actuated by a vibration energy field," *Sens. Actuators A, Phys.*, vol. 43, no. 3, pp. 366–370, May 1994.

[6] A. Cox, D. Monopoli, D. Cveticanin, M. Goldfarb, and E. Garcia, "The development of elastodynamic components for piezoelectrically actuated flapping micro-air vehicles," *J. Intell. Mater. Syst. Struct.*, vol. 13, pp. 611–615, Sep. 2002.

[7] S.S. Baek, K.Y. Ma, and R.S. Fearing, "Efficient resonant drive of flapping-wing robots," in *Proc. IEEE/RSJ Int. Conf. Intell. Robot. Syst.*, St. Louis, MO, Oct. 11–15, 2009, pp. 2854–2860.

[8] Delfly. [Online]. Available: http://www.delfly.nl

[9] Z. A. Khan and S. K. Agrawal, "Design of flapping mechanisms based on transverse bending phenomena in insects," in *Proc. IEEE Int. Conf. Robot. Autom.*, Orlando, FL, May 15–19, 2006, pp. 2323–2328.

[10] L. Schenato, D. Campolo, and S. Sastry, "Controllability issues in flapping flight for biomimetic micro aerial vehicles (MAVs)," in *Proc. IEEE Conf. Decis. Control*, vol. 6, Maui, HI, Dec. 9–12, 2003, pp. 6441–6447.

[11] R. Madangopal, Z. A. Khan, and S. K. Agrawal, "Biologically inspired design of small flapping wing air vehicles using four-bar mechanisms and quasi-steady aerodynamics," *J. Mech. Des.*, vol. 127, pp. 809–816, Jul. 2005.

[12] T. Weis-Fogh, "Quick estimates of flight fitness in hovering animals, including novel mechanisms for lift production," *J. Exp. Biol.*, vol. 59, no. 1, pp. 169–230, Aug. 1973.

[13] L. Zhao, Q. Huang, X. Deng, and S. P. Sane, "Aerodynamic effects of flexibility in flapping wings," *J. Roy. Soc. Interface.*, vol. 7, no. 44, pp. 485–497, Mar. 2010.

[14] D. Campolo, "Motor selection via impedance-matching for driving nonlinearly damped, resonant loads," *Mechatronics*, vol. 20, no. 5, pp. 566–573, Aug. 2010.

[15] S. L. Lindstedt, T. E. Reich, P. Keim, and P. C. Lastayo, "Do muscles function as adaptable locomotor springs?," *J. Exp. Biol.*, vol. 205, no. 15, pp. 2211–2216, Aug. 2002.

[16] Precision Microdrives. [Online]. Available: http://www.precision-microdrives.com

[17] C. P. Ellington, "The aerodynamics of hovering insect flight. VI. Lift and power requirements," *Philos. Trans. R. Soc. B*, vol. 305, no. 1122, pp. 145–181, Feb. 1984.

[18] F. van Breugel, Z. E. Teoh, and H. Lipson, "A passively stable hovering flapping micro-air vehicle," in *Flying Insects and Robots*, D. Floreano, J.-C. Zufferey, M. V. Srinivasan, and C. Ellington, Eds. Berlin, Germany: Springer-Verlag, 2009, vol. 13, pp. 171–184.

[19] M. Sitti, D. Campolo, J. Yan, and R.S. Fearing, "Development of PZT and PZN-PT based unimorph actuators for micromechanical flapping mechanisms," in *Proc. IEEE Int. Conf. Robot. Autom.*, Seoul, Korea, May 21–26, 2001, pp. 3839–3846.

Domenico Campolo received the Laurea degree (Hons.) in electrical and electronics engineering from the University of Pisa, Pisa, Italy, in 1998, and the Ph.D. degree in micro-engineering from the Scuola Superiore Sant'Anna, Pisa.

From 2000 to 2003, he was at the University of California-Berkeley as a Visiting Scholar, where in 2002, he was involved in postdoctoral research on the Micromechanical Flying Insect project. From 2003 to 2008, he was at Campus Bio-Medico University, Rome, Italy, as a Researcher. Since 2009, he has been an Assistant Professor in the School of Mechanical and Aerospace Engineering, Nanyang Technological University, Singapore. His research interests include bioinspired robotics and neuroscience.

Dr. Campolo is an Associate Editor of the *Journal of Micro-Bio Robotics*.

Muhammad Azhar received the B.Eng. degree in aeronautics and astronautics from the Institut Teknologi Bandung, Bandung, Indonesia, in 2007, and the M.Sc. degree in advanced technology fusion from Konkuk University, Seoul, Korea, in 2009. He is currently working toward the Ph.D. degree at Nanyang Technological University, Singapore.

From 2010 to 2011, he was a Research Associate at the Robotics Research Centre, Nanyang Technological University.

Gih-Keong Lau received the Bachelor's and Master's degrees in mechanical engineering from Nanyang Technological University, Singapore, in 1998 and 2001, respectively, and the Ph.D. degree in mechanical engineering from Delft University of Technology, Delft, The Netherlands, in 2007.

Since 2008, he has been an Assistant Professor with the School of Mechanical and Aerospace Engineering, Nanyang Technological University. His research interests include the areas of microactuators, microfabrication technology, electroactive polymers, topology optimization, compliant mechanisms, and micro-air vehicles.

Metin Sitti (S'94–M'00–SM'08) received the B.Sc. and M.Sc. degrees in electrical and electronics engineering from Bogazici University, Istanbul, Turkey, in 1992 and 1994, respectively, and The Ph.D. degree in electrical engineering from The University of Tokyo, Tokyo, Japan, in 1999.

He was a Research Scientist with the University of California at Berkeley during 1999–2002. He is currently a Professor with the Department of Mechanical Engineering and Robotics Institute, Carnegie Mellon University, Pittsburgh, PA. His research interests include micro/nanorobotics, bioinspired and biohybrid miniature mobile robots, and micro/nanomanipulation.

Dr. Sitti received the SPIE Nanoengineering Pioneer Award in 2011. He was appointed as the Adamson Career Faculty Fellow during 2007–2010. He was the Vice President for Technical Activities of the IEEE Nanotechnology Council during 2008–2010. He was elected as a Distinguished Lecturer of the IEEE Robotics and Automation Society for 2006–2008. He received a National Science Foundation CAREER Award and the Struminger Award in 2005. He has received many Best Paper and Video Awards at major robotics conferences. He is the Co-Editor-In-Chief of the *Journal of Micro-Bio Robotics*.